Biophysical Reports

LETTER

Surface tension and viscosity of protein condensates quantified by micropipette aspiration

Huan Wang,[1] Fleurie M. Kelley,[2] Dragomir Milovanovic,[3] Benjamin S. Schuster,[2] and Zheng Shi[1,*]
[1]Department of Chemistry and Chemical Biology and [2]Department of Chemical and Biochemical Engineering, Rutgers University, Piscataway, New Jersey; and [3]Laboratory of Molecular Neuroscience, German Center for Neurodegenerative Diseases, Berlin, Germany

ABSTRACT The material properties of biomolecular condensates have been suggested to play important biological and pathological roles. Despite the rapid increase in the number of biomolecules identified that undergo liquid-liquid phase separation, quantitative studies and direct measurements of the material properties of the resulting condensates have been severely lagging behind. Here, we develop a micropipette-based technique that uniquely, to our knowledge, allows quantifications of both the surface tension and viscosity of biomolecular condensates, independent of labeling and surface-wetting effects. We demonstrate the accuracy and versatility of this technique by measuring condensates of LAF-1 RGG domains and a polymer-based aqueous two-phase system. We further confirm our measurements using established condensate fusion and fluorescence recovery after photobleaching assays. We anticipate the micropipette-based technique will be widely applicable to biomolecular condensates and will resolve several limitations regarding current approaches.

WHY IT MATTERS Biomolecular condensates that arise from liquid-liquid phase separation are often likened to oil droplets in water because of the coexistence of two liquid phases without a membrane boundary. However, oil droplets and biomolecular condensates represent two extremes in the realm of liquid properties. The surface tension of oil droplets is ~1000 times higher, whereas their viscosity is ~1000 times lower, compared with biomolecular condensates. The unique combination of high viscosity and low surface tension makes biomolecular condensates well suited for quantitative micropipette aspiration studies, as demonstrated in this study using condensates of LAF-1 RGG domains. Compared to oil droplets, biomolecular condensates more closely resemble a polymer-based aqueous two-phase system, illustrating how knowledge in polymer physics can guide mechanistic understanding of phase separation in biology.

INTRODUCTION

Biomolecular condensates that arise from liquid-liquid phase separation (LLPS) have recently emerged as a central player in numerous cellular processes (1,2). Surface tension and viscosity are two independent parameters that define the material properties of a liquid (3,4). Gradual increases in the viscosities of biomolecular condensates are often linked to the formation of fibrils that underlie aging-associated diseases (5–10). Quantification of condensate rheology therefore holds promise for unraveling the mechanisms, as well as facilitating therapeutic advances in the treatment of these diseases (11).

The surface tension of biomolecular condensates can also play key physiological roles. Differences in surface tension can lead to layered multiphase condensates, such as the compartmentation in nucleoli (12–14). During autophagy, surface tension determines whether p62 condensates will be sequestered in small droplets or digested as a whole (15). Finally, the nucleation of microtubule branches relies on an instability of TPX2 condensates, driven solely by the condensates' surface tension (16).

Several techniques have been developed to probe either the viscosity or the surface tension of biomolecular condensates (8,12,17–21). The most widely used measure of viscosity relies on fluorescence recovery after photobleaching (FRAP), which is challenging to quantify in the scenario of three-dimensional compartments such as biomolecular condensates (4,22). Measurements of surface tension rely heavily on the fusion kinetics between two condensates (17). Although significant improvements have been made (23,24), the fusion assay is intrinsically limited because only a ratio of surface tension/viscosity can be estimated (12). Therefore,

Submitted June 21, 2021, and accepted for publication July 26, 2021.
*Correspondence: zheng.shi@rutgers.edu
Editor: Erdinc Sezgin.
https://doi.org/10.1016/j.bpr.2021.100011

a user-friendly technique that can directly measure both the surface tension and the viscosity of biomolecular condensates is still missing.

Micropipette aspiration (MPA) has been well established to study the elasticities of liposomes (25,26), polymersomes (27,28), and cells (29,30). However, it has been challenging to apply MPA to quantify liquids. Dimensional analyses on typical MPA experiments show that precise quantifications of both the viscosity and surface tension can only be achieved on liquids with viscosity values (in Pa · s) larger than 2% of their surface tension values (in mN/m) (see Supporting materials and methods for details). Although the criteria is not met by common oil droplets (viscosity: 10^{-3}–10^{-2} Pa · s; surface tension: ~10 mN/m), currently available data suggest that biomolecular condensates and certain aqueous two-phase systems (ATPSs) (viscosity: 10^{-1}–10^{3} Pa · s; surface tension: 10^{-4}–10^{-1} mN/m) are well poised for quantitative MPA studies (Fig. 1).

Here, we demonstrate the application of MPA to quantify the viscosity and surface tension of liquid condensates. We calibrated our method using a PEG-dextran ATPS (35). This allowed us to develop a linear model to extract the material properties of condensates from their responses to MPA. We applied this technique to quantify condensates formed by the RGG domain, a well-known RNA binding region of the P granule RNA helicase LAF-1 that undergoes LLPS (18,36). We further confirmed our viscosity and surface tension measurements by FRAP and fusion assays, respectively. Our results suggest that the material properties of protein condensates are closer to the ATPS than to oil droplets in water. MPA represents an active microrheology technique that can simultaneously quantify independent properties of biomolecular condensates, insensitive to common sources of artifacts such as labeling, photobleaching, and wetting effects of proteins.

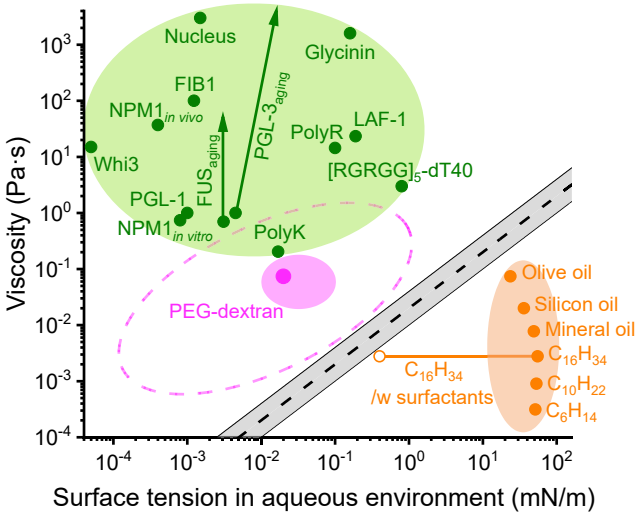

FIGURE 1 Viscosity and surface tension of liquids. Viscosity and surface tension of biomolecular condensates in aqueous buffer (*green*, *arrows* represent changes of properties over time) and common "oil droplets" in water are shown (*orange*, *open circle* and *line* represent the minimum and change of hexadecane surface tension in the presence of surfactants (31)). The gray belt represents an estimated boundary above which MPA will be well suited for viscosity and surface tension measurements ($\eta = 0.02\times\gamma$ is plotted as the *black dashed line*; the *gray region* represents $\eta = 0.01\times\gamma$ to $\eta = 0.04\times\gamma$; see Supporting materials and methods for details). Viscosity and surface tension of the dextran-rich condensates (in PEG-dextran ATPS) measured in this study are shown as the magenta circle. Literature values for dextran-rich condensates are represented by the dashed circle (32–34), with compositions comparable with the one used in this study highlighted in light magenta. See Table S1 for values and references used in this plot.

Results

Calibration of MPA with PEG-dextran ATPS

To study the relation between the stress and strain rate of a liquid, a critical aspiration pressure P_γ, determined by the surface tension (γ) of the condensate, needs to be reached. At aspiration pressures (P_{asp}) greater than P_γ, the condensate will flow into the micropipette (Fig. 2 *a*; we define suction pressures as positive). For a Newtonian fluid, the pressure difference and the shear rate are linearly related via the condensate's viscosity (η) (37):

$$P_{asp} = M \times \eta \times S + P_\gamma. \quad (1)$$

Here, M is a unitless dissipation factor that corresponds to the radial collapse of the condensate during aspiration (37), $S = d(L_p/R_p)/dt$ is the shear rate, L_p is the aspiration length, and R_p is the radius of the micropipette. The critical pressure is $P_\gamma = 2\gamma(H - 1/R_c)$, with H representing the mean curvature of the liquid interface in the micropipette (we define the curvature illustrated in Fig. 2 *a* as positive). The unaspirated portion of the condensate is approximated by a sphere of radius R_c. Equation 1 is valid when $\Delta L_p R_p^2/R_c^3 << 1$, with M independent of geometrical factors in the MPA system (37). When $\Delta L_p R_p^2/R_c^3 \sim 1$, geometrical dependence of M and dissipation in the micropipette will need to be considered. In our experiments, $\Delta L_p R_p^2/R_c^3 < 0.05$.

R_c, L_p, R_p, and H describe the shape of the aspirated condensate and are readily available through microscopy. However, the unitless dissipation constant M must be determined experimentally by aspirating liquids of known viscosities (37). Then, by measuring S under different P_{asp}, the viscosity and surface tension of an unknown liquid condensate can be quantified from the slope and intercept, respectively, of Eq. 1.

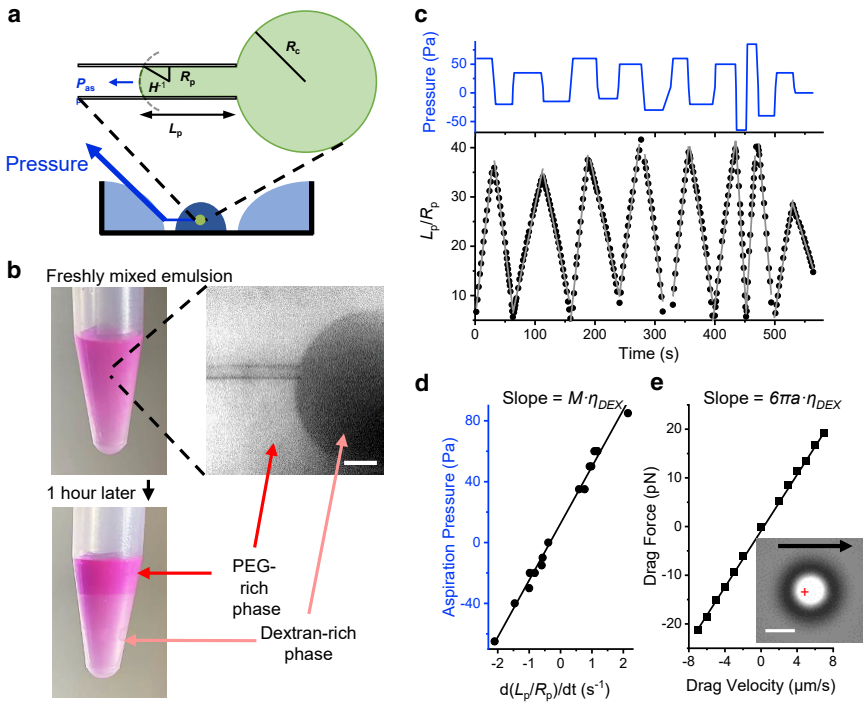

FIGURE 2 Micropipette aspiration of dextran-rich condensates. (*a*) Illustration of the micropipette aspiration system: dark blue, sample; light blue, water used for minimizing evaporation; green, a pipette-aspirated condensate; P_{asp}, aspiration pressure; R_p, pipette radius; L_p, aspiration length; R_c, radius of condensate outside the pipette. H: mean curvature of the liquid interface in the micropipette. (*b*) An emulsion of PEG-dextran (*upper*) undergoes bulk LLPS after creaming for 1 h (*lower*). Scale bars, 20 μm. (*c*) Aspiration pressure (*upper*) and normalized aspiration length (*lower*) during MPA. Gray lines: linear fits of the normalized aspiration length for each pressure step. (*d*) P_{asp} of each step plotted against the corresponding shear rate (slopes of the *gray lines* in *c*). (*e*) Viscosity determination by optical dragging. Inset image: a trapped polystyrene particle dragged at 5 μm/s (*arrow*) in the dextran-rich phase. Cross: trap-center. Scale bars, 2 μm. Linear fits: $R^2 = 0.990$ for (*d*) and 0.999 for (*e*).

To calibrate M with liquids that are appropriate for MPA (Fig. 1), we chose an ATPS composed of PEG (8000 Da) and dextran (500,000 Da) (15,32,38). Under a range of concentrations, mixtures of PEG and dextran will phase separate into emulsions of micrometer-sized droplets (Fig. S1 *a*). Rhodamine-B was included to identify the condensates microscopically. This mixture produced a labeled emulsion that is stable on the timescale of MPA experiments (~10 min) but undergoes bulk phase separation after 1–2 h (Fig. 2 *b*).

With careful control of water evaporation (Fig. S2), next we applied MPA to samples of limited volumes (20–30 μL). Stepwise aspiration pressures were applied to dextran-rich condensates, and the aspiration length was found to change linearly under each pressure step (Figs. 2 *c* and S1 *b*). The resulting relation between the aspiration pressure and the condensate flow (Fig. 2 *d*) agrees well with predictions from Eq. 1. The slope $dP_{asp}/dS = 37.0 \pm 0.7$ Pa · s (n = 6; mean ± standard error of the mean for all values reported herein) represents the viscosity of the dextran-rich phase multiplied by M (Eq. 1). We then directly measured the viscosity by dragging an optically trapped particle within the dextran-rich phase (Fig. 2 *e*). The measured viscosity of the dextran-rich phase (74 ± 4 mPa · s) agreed with bulk viscometer measurements (Supporting materials and methods), giving $M = 500 \pm 30$, a value that can be directly applied when quantifying the viscosity of other liquid condensates via independent MPA setups, provided $\Delta L_p R_p^2/R_c^3 << 1$. Additionally, the intercept from the P_{asp}-S relation corresponds to a surface tension of 0.02 ± 0.01 mN/m (Eq. 1), in agreement with the literature (32,34).

Surface tension and viscosity of LAF-1 RGG condensates quantified by MPA

LAF-1 is one of the first well-studied proteins that undergoes LLPS, mediated mainly by its intrinsically disordered N-terminal RGG domain (4,18,19,22,36). The RGG domain consists of the first 168 residues of LAF-1 and is especially rich in glycine and arginine (39). We applied MPA to a tandem RGG domain that robustly undergoes LLPS (Supporting materials and methods; hereafter named RGG condensates) (36). Unlike dextran-rich condensates, RGG condensates fully wet the inner wall of the micropipette, requiring a negative (ejection) pressure P_γ to balance the capillary effect (Fig. 3 *a*; Video S1; $H \approx -1/R_p$). Beyond P_γ, the aspiration length changed linearly under each pressure step (Fig. 3 *b*), indicating a lack of condensate elasticity at the timescale we were probing (>1 s). After the initial entry steps, the shear rate S increased linearly with P_{asp} (Figs. 3 *c*, S3, and S4). The slope corresponded to a viscosity of 1.62 ± 0.18 Pa · s (n = 11). As expected from the wetting behavior, the intercept of P_{asp} vs. S was negative, and the corresponding surface tension was 0.159 ± 0.010 mN/m (n = 11). The viscosity and surface tension measured through MPA are in agreement with previous estimates for condensates of LAF-1 RGG using FRAP and condensate fusion assays (39).

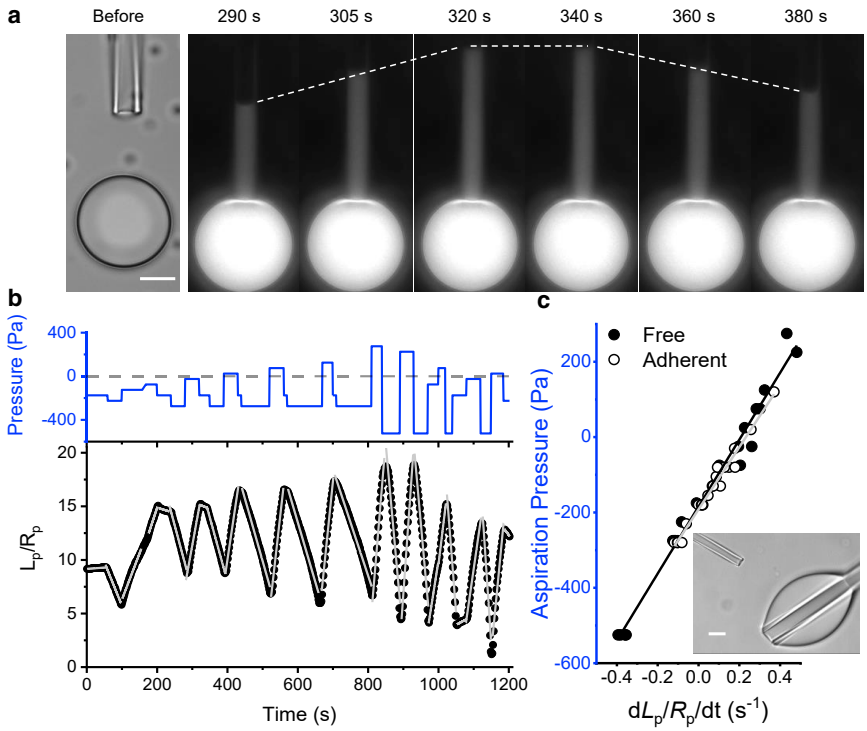

FIGURE 3 MPA of RGG condensates. (*a*) Left: transmitted light image of an RGG condensate with a nearby micropipette. Right: time-lapse fluorescent images of the RGG condensate under three aspiration pressures: −25 Pa (290–320 s), −175 Pa (320–340 s), and −275 Pa (340–380 s). Dashed lines trace the change of L_p. (*b*) Aspiration pressure (*upper*) and normalized aspiration length (*lower*) during MPA. Dashed line: zero pressure. Gray lines: linear fits of the normalized aspiration length for each pressure step. (*c*) P_{asp} of each step plotted against the corresponding shear rates for a free condensate (*closed*, see *a*) and a condensate strongly adhered to a glass pipette (*open*, *inset image*). Linear fits to the data are shown as black (slope: 890 ± 30 Pa · s, intercept: −184 ± 7 Pa, R^2 = 0.982) and gray (slope: 830 ± 30 Pa · s, intercept: −192 ± 4 Pa, R^2 = 0.976) lines, respectively. All scale bars, 10 μm.

Compared with currently available methods for condensate rheology and surface tension measurements, MPA has significant advantages. First, many proteins tend to wet and adsorb onto solid surfaces (4,16,23,24,40). Although potentially mediating important biological processes (15,16,40,41), this wetting effect can introduce significant artifacts in measurements that rely on the fusion kinetics or morphology of condensates (12,23,24). In our experiments, adhesion between RGG condensates and the glass bottom dish can be prevented by coating the glass with Pluronic F-127 (36). However, the same coating procedure does not necessarily work for other protein condensates or glass surfaces. To study the effect of wetting in MPA measurements, we carried out experiments to compare sedimented condensates that were weakly attached to the bottom coverglass of a coated dish (Fig. 3 *a*) with condensates that were strongly adhered to a bare glass pipette (Fig. 3 *c*, *inset*; n = 5). Adhesion to glass led to nonspherical condensates outside the aspiration pipette (Videos S2 and S3); however, P_{asp} vs. S relations measured under these two different configurations were not significantly different (Fig. 3 *c*; p = 0.83 for viscosity and p = 0.45 for surface tension, Student's *t*-test). The insensitivity of MPA to the wetting between condensate and glass is expected from Eq. 1, for which the contribution of R_c is negligible when $|R_c^{-1}| << H$, as in our experiments. Additionally, fluorescent labeling of the protein is not necessary for MPA as long as the condensate-buffer interfaces can be resolved (Figs. S1 *c* and S4; Video S3). For the same reasons, MPA measurements are insensitive to photobleaching and can be easily combined with fluorescence-based studies (24,42). Finally, MPA does not require highly specialized instrumentation or the incorporation particles to the condensate (8,18), further expanding the applicability of this technique.

Estimation of RGG condensate properties through FRAP and fusion assays

To confirm the accuracy of the surface tension and viscosity of RGG condensates measured by MPA, we first adopted an improved version of the condensate fusion assay (23,24). Two optically trapped RGG condensates were manipulated to encounter each other, and the subsequent fusion process was recorded (Fig. 4, *a and b*; n = 76 pairs). A linear relation was observed between the fusion time and the size of the condensates (Fig. 4 *c*). The slope, which scales with the inverse capillary velocity η/γ, was 0.016 ± 0.002 s/μm, in agreement with the MPA measurements (η/γ = 0.010 ± 0.001 s/μm).

We then used FRAP to estimate the viscosity of RGG condensates. A circular region within RGG condensates was photobleached, and the three-dimensional diffusion coefficient (D = 0.018 μm^2/s) was calculated based on the half-recovery time (Fig. 4 *d*, n = 42; Eqs. S7a and S8b) (22). Combined with an estimate of the protein hydrodynamic radius, we obtained a viscosity

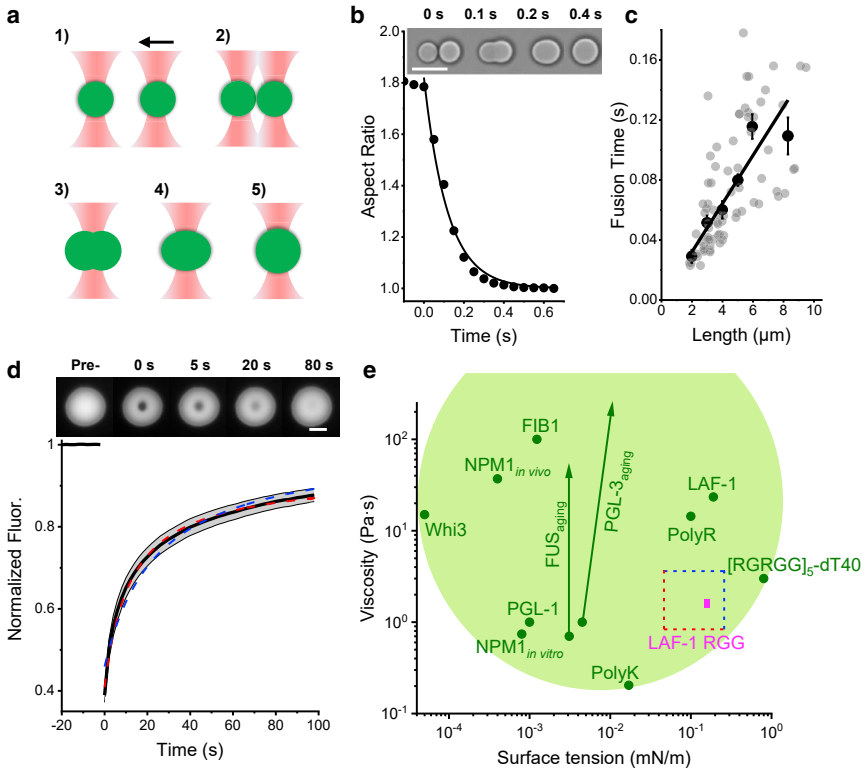

FIGURE 4 Surface tension and viscosity of RGG condensates estimated from condensate fusion and FRAP. (*a*) (*1–5*): Illustration of the condensate fusion experiment using dual-optical traps. (*b*) Fusion of two RGG condensates (*inset images*) quantified as a decrease of the overall aspect ratio to 1. The curve is an exponential fit. (*c*) The fusion time of RGG condensates versus the condensates' length. Gray and black circles are individual and binned fusion experiments, respectively. Line: weighted linear fit to the binned data ($R^2 = 0.902$). (*d*) FRAP measurements within RGG condensates. Inset images show a representative experiment. Red dash represents the fit to a model in which an immobile fraction of the protein was allowed (Eq. S7a; $R^2 = 0.995$). Blue dash represents the fit to a model in which all proteins were assumed to be mobile (Eq. S7b; $R^2 = 0.966$). (*e*) Zoom-in of Fig. 1, with MPA-measured RGG condensate viscosity (1.62 ± 0.18 Pa · s) and surface tension (0.159 ± 0.010 mN/m) represented by the magenta box. The range of viscosity and surface tension estimated from FRAP and condensate fusion are represented by the dashed box. The horizontal red dashed line ($\eta = 0.8$ Pa · s) represents viscosity calculated assuming the presence of immobile proteins in a two-dimensional model (Eqs. S7a and S8a). The vertical red dashed line represents surface tension calculated using $\eta = 0.8$ Pa · s and the upper bound of inverse capillary velocity ($\eta/\gamma = 0.018$ s/μm). The horizontal blue dashed line ($\eta = 3.6$ Pa · s) represents viscosity calculated assuming the absence of immobile fraction in a three-dimensional model (Eqs. S7b and S8b). The vertical blue dashed line represents surface tension calculated using $\eta = 3.6$ Pa · s and the lower bound of inverse capillary velocity ($\eta/\gamma = 0.014$ s/μm). All error bars are mean $\pm$ standard error of the mean; all scale bars represent 10 μm.

of 1.8 Pa · s, comparable with the MPA result. We noticed that viscosity values between 0.8 and 3.6 Pa · s can be extracted from FRAP, depending on the extract model of choice (Fig. 4 *e*). The agreement between FRAP- and MPA-based viscosity measurements on the same RGG condensates independently confirmed that our calibrated *M* value (500 $\pm$ 30) is accurate within a factor of 2.

Discussion

In this study, we only explored condensates that behave as Newtonian fluids at the timescale of our MPA measurements (>1 s). We demonstrated that MPA can be applied to simultaneously quantify the surface tension and viscosity of RGG condensates. However, several other biomolecule condensates are known to be viscoelastic or gel-like (8,10,20). When applying stepwise changes in aspiration pressure to viscoelastic condensates, immediate elastic responses followed by nonlinear creep compliances in the aspiration length would be expected (43). Although these were not observed on either dextran-rich (Fig. 2 *c*) or RGG condensates (Fig. 3 *b*), it is highly probable that condensates made of complex multidomain proteins can exhibit prominent viscoelastic features. Generalized viscoelastic models will need to be evoked to fit the time-dependent aspiration lengths when applying our MPA protocol to viscoelastic condensates. Specifically, this involves replacing the linear fitting to the aspiration length (such as in the *lower panels* of Figs. 2 *c* and 3 *b*) with exponential or power-law fittings (44). It is also possible to apply a sinusoidally oscillating pressure to an aspirated condensate, for which the phase delay in the response of aspiration length will inform the condensate's frequency-dependent viscoelasticity (20,45). Because of the inertia of the aspiration system, it is challenging to operate MPA faster than 10 Hz. However, it is currently unclear whether the high-frequency elastic response of biomolecular condensates would have direct biological relevance.

RGG condensates fuse quickly (inverse capillary velocity ~0.01 s/μm) with >90% of the constituting proteins moving freely, consistent with their liquid behavior during MPA. However, many biomolecular condensates can take more than 100 s to fuse (15,46) while exhibiting small fractions (<50%) of mobile proteins (3,10,47). In the latter cases, MPA measurements will be essential to clarify confusion

around the condensates' material properties. For example, in a “gel-like” multicomponent condensate (10), viscoelastic properties of the condensate can be measured by MPA without necessarily knowing its molecular constituents, in contrast with assays based on fluorescent labeling.

The unambiguous quantification of RGG condensates through MPA further iterates the contrasting material properties of biomolecular condensates and oil droplets (Fig. 1). For example, mineral oil has a surface tension 300-fold higher than that of RGG condensates, whereas its viscosity is more than 200-fold lower. The cause of this drastic difference between biomolecular condensates and oil droplets has not been studied in detail. However, it is conceivable that the large size of biopolymers compared with those of typical oil molecules plays a role in determining both viscosity and surface tension (17). The difference can also arise from intermolecular interactions. For example, the strong hydrophobicity of oil-like molecules contributes to their high (10 mN/m) surface tensions, whereas biopolymers often tend to form hydrogen bonds with water (48).

The contrast between biomolecular condensates and oil droplets can affect scientists' intuition about phase separation in biology; the known capillary velocities for biomolecular condensates have a median value of 1 μm/s, with several examples below 0.01 μm/s (Fig. 4 *e*). These capillary velocities correspond to a complete fusion between micron-sized condensates in seconds to minutes. These fusion rates can leave a strong impression of liquid-like condensates when observed under a microscope. However, the liquid behavior becomes nonintuitive when these micron-sized condensates are scaled to the macroscopic world. For example, under a capillary velocity of 0.01–1 μm/s, it will take hours to weeks for droplets of centimeter size to fuse together, a rate at which the liquidity of the droplets may become debatable (49).

In our protein condensates, the helicase domain and disordered C-terminal prion-like domain of the full length LAF-1 were replaced by a second copy of the N-terminal RGG domain (36). Comparing our measurements of RGG condensates and literature reports on LAF-1 condensates (18), the viscosity of RGG condensates is more than 10-fold smaller than that of LAF-1 condensates, whereas their surface tensions are comparable (Fig. 4 *e*). These results point to a potential role of the helicase and C-terminal domains in uniquely controlling the viscosity of LAF-1 condensates. More generally, surface tension and viscosity are tunable through intermolecular interactions. Thus, a future direction will be to systematically dissect how protein sequence and biochemical environment affect the material properties of biomolecular condensates (50).

Importantly, by carefully implementing a whole-cell patch-clamp configuration (51), the demonstrated MPA protocol could be applied to study large (>2 μm in diameter) cytosolic biomolecular condensates *in vivo*. MPA setups are readily available in electrophysiology and biomechanics labs, making it easily adaptable for studying the material properties of biomolecular condensates in the broader biological and chemical communities.

SUPPORTING MATERIAL

Supporting material can be found online at https://doi.org/10.1016/j.bpr.2021.100011.

AUTHOR CONTRIBUTIONS

Z.S., B.S.S., and D.M. conceived the project. H.W. and Z.S. carried out the experiments and analyzed the data. F.M.K. purified the proteins. Z.S., H.W., B.S.S., and D.M. wrote the manuscript.

ACKNOWLEDGMENTS

We thank Howard Stone and Lin Guo for critical evaluation of the manuscript. We thank Ehsan Ateﬁ, Ningwei Li, Rumiana Dimova, Christine Keating, Dennis Discher, Marina Feric, Roland Knorr, Frank Jülicher, and Rick Remsing for helpful discussions. We thank Gayatri Ganeshan, Steven Arnold, and Roberto Sul for careful proofreading. We also thank Andy Nieuwkoop and his lab for helping with materials and storage space.

Z.S. and B.S.S. are supported by Rutgers University startup funds. F.M.K. is supported by National Institutes of Health Award T32 GM135141. D.M. is supported by the German Research Foundation (MI 2104 and SFB 1286) and the German Academic Exchange Service (PPE 2021).

DECLARATION OF INTERESTS

The authors declare no competing interests.

REFERENCES

1. Shin, Y., and C. P. Brangwynne. 2017. Liquid phase condensation in cell physiology and disease. *Science.* 357:eaaf4382.
2. Banani, S. F., H. O. Lee, …, M. K. Rosen. 2017. Biomolecular condensates: organizers of cellular biochemistry. *Nat. Rev. Mol. Cell Biol.* 18:285–298.
3. Bracha, D., M. T. Walls, and C. P. Brangwynne. 2019. Probing and engineering liquid-phase organelles. *Nat. Biotechnol.* 37:1435–1445.
4. Schuster, B. S., R. M. Regy, …, J. Mittal. 2021. Biomolecular condensates: sequence determinants of phase separation, microstructural organization, enzymatic activity, and material properties. *J. Phys. Chem. B.* 125:3441–3451.
5. Mathieu, C., R. V. Pappu, and J. P. Taylor. 2020. Beyond aggregation: pathological phase transitions in neurodegenerative disease. *Science.* 370:56–60.

6. Nedelsky, N. B., and J. P. Taylor. 2019. Bridging biophysics and neurology: aberrant phase transitions in neurodegenerative disease. *Nat. Rev. Neurol.* 15:272–286.
7. Alberti, S., and D. Dormann. 2019. Liquid–liquid phase separation in disease. *Annu. Rev. Genet.* 53:171–194.
8. Jawerth, L., E. Fischer-Friedrich, …, F. Jülicher. 2020. Protein condensates as aging Maxwell fluids. *Science.* 370:1317–1323.
9. Guo, L., H. J. Kim, …, J. Shorter. 2018. Nuclear-import receptors reverse aberrant phase transitions of RNA-binding proteins with prion-like domains. *Cell.* 173:677–692.e20.
10. Putnam, A., M. Cassani, …, G. Seydoux. 2019. A gel phase promotes condensation of liquid P granules in *Caenorhabditis elegans* embryos. *Nat. Struct. Mol. Biol.* 26:220–226.
11. Guo, L., C. M. Fare, and J. Shorter. 2019. Therapeutic dissolution of aberrant phases by nuclear-import receptors. *Trends Cell Biol.* 29:308–322.
12. Feric, M., N. Vaidya, …, C. P. Brangwynne. 2016. Coexisting liquid phases underlie nucleolar subcompartments. *Cell.* 165:1686–1697.
13. Fisher, R. S., and S. Elbaum-Garfinkle. 2020. Tunable multiphase dynamics of arginine and lysine liquid condensates. *Nat. Commun.* 11:4628.
14. Yu, H., S. Lu, …, D. W. Cleveland. 2021. HSP70 chaperones RNA-free TDP-43 into anisotropic intranuclear liquid spherical shells. *Science.* 371:eabb4309.
15. Agudo-Canalejo, J., S. W. Schultz, …, R. L. Knorr. 2021. Wetting regulates autophagy of phase-separated compartments and the cytosol. *Nature.* 591:142–146.
16. Setru, S. U., B. Gouveia, …, S. Petry. 2021. A hydrodynamic instability drives protein droplet formation on microtubules to nucleate branches. *Nat. Phys.* 17:493–498.
17. Brangwynne, C. P., C. R. Eckmann, …, A. A. Hyman. 2009. Germline P granules are liquid droplets that localize by controlled dissolution/condensation. *Science.* 324:1729–1732.
18. Elbaum-Garfinkle, S., Y. Kim, …, C. P. Brangwynne. 2015. The disordered P granule protein LAF-1 drives phase separation into droplets with tunable viscosity and dynamics. *Proc. Natl. Acad. Sci. USA.* 112:7189–7194.
19. Taylor, N., S. Elbaum-Garfinkle, …, C. P. Brangwynne. 2016. Biophysical characterization of organelle-based RNA/protein liquid phases using microfluidics. *Soft Matter.* 12:9142–9150.
20. Jawerth, L. M., M. Ijavi, …, E. Fischer-Friedrich. 2018. Salt-dependent rheology and surface tension of protein condensates using optical traps. *Phys. Rev. Lett.* 121:258101.
21. Caragine, C. M., S. C. Haley, and A. Zidovska. 2018. Surface fluctuations and coalescence of nucleolar droplets in the human cell nucleus. *Phys. Rev. Lett.* 121:148101.
22. Taylor, N. O., M. T. Wei, …, C. P. Brangwynne. 2019. Quantifying dynamics in phase-separated condensates using fluorescence recovery after photobleaching. *Biophys. J.* 117:1285–1300.
23. Alshareedah, I., G. M. Thurston, and P. R. Banerjee. 2021. Quantifying viscosity and surface tension of multicomponent protein-nucleic acid condensates. *Biophys. J.* 120:1161–1169.
24. Ghosh, A., and H. X. Zhou. 2020. Determinants for fusion speed of biomolecular droplets. *Angew. Chem. Int. Ed. Engl.* 59:20837–20840.
25. Shi, Z., and T. Baumgart. 2015. Membrane tension and peripheral protein density mediate membrane shape transitions. *Nat. Commun.* 6:5974.
26. Evans, E., and W. Rawicz. 1990. Entropy-driven tension and bending elasticity in condensed-fluid membranes. *Phys. Rev. Lett.* 64:2094–2097.
27. Luo, Q., Z. Shi, …, S. J. Park. 2016. DNA island formation on binary block copolymer vesicles. *J. Am. Chem. Soc.* 138:10157–10162.
28. Discher, B. M., Y. Y. Won, …, D. A. Hammer. 1999. Polymersomes: tough vesicles made from diblock copolymers. *Science.* 284:1143–1146.
29. Hochmuth, R. M. 2000. Micropipette aspiration of living cells. *J. Biomech.* 33:15–22.
30. Lee, L. M., and A. P. Liu. 2014. The application of micropipette aspiration in molecular mechanics of single cells. *J. Nanotechnol. Eng. Med.* 5:0408011–0408016.
31. Chen, H., L. Han, …, Z. Ye. 2004. The interfacial tension between oil and gemini surfactant solution. *Surf. Sci.* 552:L53–L57.
32. Atefi, E., J. A. Mann, Jr., and H. Tavana. 2014. Ultralow interfacial tensions of aqueous two-phase systems measured using drop shape. *Langmuir.* 30:9691–9699.
33. Carrasco, F., E. Chornet, …, J. Costa. 1989. A generalized correlation for the viscosity of dextrans in aqueous solutions as a function of temperature, concentration, and molecular weight at low shear rates. *J. Appl. Polym. Sci.* 37:2087–2098.
34. Liu, Y., R. Lipowsky, and R. Dimova. 2012. Concentration dependence of the interfacial tension for aqueous two-phase polymer solutions of dextran and polyethylene glycol. *Langmuir.* 28:3831–3839.
35. Crowe, C. D., and C. D. Keating. 2018. Liquid-liquid phase separation in artificial cells. *Interface Focus.* 8:20180032.
36. Schuster, B. S., E. H. Reed, …, D. A. Hammer. 2018. Controllable protein phase separation and modular recruitment to form responsive membraneless organelles. *Nat. Commun.* 9:2985.
37. Drury, J. L., and M. Dembo. 1999. Hydrodynamics of micropipette aspiration. *Biophys. J.* 76:110–128.
38. Helfrich, M. R., L. K. Mangeney-Slavin, …, C. D. Keating. 2002. Aqueous phase separation in giant vesicles. *J. Am. Chem. Soc.* 124:13374–13375.
39. Schuster, B. S., G. L. Dignon, …, J. Mittal. 2020. Identifying sequence perturbations to an intrinsically disordered protein that determine its phase-separation behavior. *Proc. Natl. Acad. Sci. USA.* 117:11421–11431.
40. Su, X., J. A. Ditlev, …, R. D. Vale. 2016. Phase separation of signaling molecules promotes T cell receptor signal transduction. *Science.* 352:595–599.
41. Milovanovic, D., Y. Wu, …, P. De Camilli. 2018. A liquid phase of synapsin and lipid vesicles. *Science.* 361:604–607.
42. Alberti, S., A. Gladfelter, and T. Mittag. 2019. Considerations and challenges in studying liquid-liquid phase separation and biomolecular condensates. *Cell.* 176:419–434.
43. Mitchell, J. R. 1980. The rheology of gels. *J. Texture Stud.* 11:315–337.
44. Moazzeni, S., Y. Demiryurek, …, H. Lin. 2021. Single-cell mechanical analysis and tension quantification via electrodeformation relaxation. *Phys. Rev. E.* 103:032409.
45. Sakai, A., Y. Murayama, and M. Yanagisawa. 2020. Cyclic micropipette aspiration reveals viscoelastic change of a gelatin microgel prepared inside a lipid droplet. *Langmuir.* 36:5186–5191.
46. Zhang, H., S. Elbaum-Garfinkle, …, A. S. Gladfelter. 2015. RNA controls PolyQ protein phase transitions. *Mol. Cell.* 60:220–230.
47. Hoffmann, C., R. Sansevrino, …, D. Milovanovic. 2021. Synapsin condensates recruit alpha-synuclein. *J. Mol. Biol.* 433:166961.
48. Israelachvili, J. N. 2015. Intermolecular and Surface Forces. Academic Press, Cambridge, MA.
49. Edgeworth, R., B. J. Dalton, and T. Parnell. 1984. The pitch drop experiment. *Eur. J. Phys.* 5:198–200.
50. Peeples, W., and M. K. Rosen. 2021. Mechanistic dissection of increased enzymatic rate in a phase-separated compartment. *Nat. Chem. Biol.* 17:693–702.
51. Zhang, H., E. Reichert, and A. E. Cohen. 2016. Optical electrophysiology for probing function and pharmacology of voltage-gated ion channels. *eLife.* 5:e15202.

Biophysical Reports, Volume *1*

Supplemental information

Surface tension and viscosity of protein condensates quantified by micropipette aspiration

Huan Wang, Fleurie M. Kelley, Dragomir Milovanovic, Benjamin S. Schuster, and Zheng Shi

Materials and Methods

Estimate of the working range of MPA through dimensional analysis

In this study, we assume that condensates behave as Newtonian fluids. During micropipette aspiration of the condensate (Fig. 2a), the viscosity needs to be large in order for the camera to capture the flow process. At the same time, the surface tension needs to be small in order for the flow to start.

Assume the maximal imaging frequency is 100 Hz ($\Delta t_{\min}$ = 0.01 s), the radius of the pipette is R_p = 1 μm, and M = 500 (see Equation 1 in the main text). In order to capture liquid deformations that are on the order of pipette diameter (ΔL_p = 2 μm), the viscosity η (in Pa·s) needs to satisfy:

$$\eta > |P_{\mathrm{asp}}| \cdot \frac{R_{\mathrm{p}} \Delta t_{\min}}{M \Delta L_{\mathrm{p}}} = 10^{-5} |P_{\mathrm{asp}}| \qquad \text{(S1)}$$

The aspiration pressure needs to overcome the capillary effect caused by the surface tension γ (in mN/m). For a non-wetting ($H^{-1} = R_p$) or a perfectly wetting ($H^{-1} = -R_p$) liquid with $R_c >> R_p$:

$$|P_{\mathrm{asp}}| > \frac{2\gamma}{R_{\mathrm{p}}} = 2 \times 10^{3} \gamma \qquad \text{(S2)}$$

Combine relations S1 and S2:

$$\eta(\text{in Pa} \cdot \text{s}) > 2 \times 10^{-2}\ \gamma\ (\text{in mN/m}) \qquad \text{(S3)}$$

Therefore, relation S3 defines the regime of viscosity and surface tension where MPA is expected to perform well. In Fig. 1, η = 0.02 γ is plotted as the black dashed line, the gray region represents η = 0.01 γ ~ 0.04 γ.

Protein purification and sample preparation

RGG-based proteins were expressed recombinantly in *E. coli* and purified by affinity chromatography, as previously described *(1)*. The working protein sample contains 1 μM RGG-EGFP-RGG (molecular mass 62.1 kDa, Addgene Plasmid #124948) and 6 μM RGG-RGG (molecular mass 35.7 kDa, Addgene Plasmid #124941) in a pH 7.5 buffer containing 20 mM Tris and 150 mM NaCl.

Phase separated dextran and PEG aqueous two-phase systems were prepared by mixing different concentrations of PEG-8000 (43443-22, Alfa Aesar, US) and dextran-500k (DE132-100GM, Spectrum Chemical, US) stock solutions. The stock solutions were prepared by dissolving each polymer in Milli-Q water. Emulsions of different PEG to dextran ratios showed different distributions of droplet size (Fig. S1a). The 5% PEG and 6.4% dextran (both by mass) mixture was chosen for micropipette aspiration, because the resulting emulsion contained droplets with comparable sizes to those of the protein condensates.

Rhodamine-B (83689-1G, Sigma, USA) was added (at a final concentration of 1 μM) to the PEG-dextran mixture to distinguish the dextran phase from the PEG phase (Fig. 2b). Rhodamine-B preferentially enters the PEG-rich phase *(2)*, therefore dextran-rich condensates showed as dark droplets in a bright background in fluorescent microscopy images (Fig. 2b, upper right image). The fluorescent labeling was confirmed by the observation that after bulk LLPS, the heavier dextran-rich layer (Fig. 2b, lower layer of the lower left image) contained less Rhodamine-B compared to the lighter PEG-rich layer. The concentration of dextran in the dextran-rich layer was estimated to be ~14% by mass.

Micropipette fabrication, aspiration, and imaging

Micropipettes were pulled from glass capillaries using a pipette puller (PUL-1000, World Precision Instruments (WPI), US). The tip of the pipette was cut to an opening diameter between 1~ 5 μm and bent to ~40° using a microforge (DMF1000, WPI).

Micropipette aspiration and imaging were carried out on a Ti2-A inverted fluorescent microscope (Nikon, Japan) equipped with a motorized stage and two motorized 4-axes micromanipulators (PatchPro-5000, Scientifica, UK). A micropipette was filled with the same buffer as the protein (20 mM Tris and 150 mM NaCl, pH 7.5) using a MICROFIL needle (WPI) and subsequently mounted onto a micromanipulator. The rear end of the pipette was connected to an adjustable water reservoir. The pipette holder was then rotated so that the bent tip of the micropipette was parallel to the imaging plane. The aspiration pressure within the micropipette was controlled and recorded by adjusting the water level in the reservoir using a set of 5 ml, 20 ml, 50 ml, and 150 ml syringes connected to the reservoir.

The zero pressure of the system was calibrated before each MPA experiment, using a dilute solution of fluorescent nanoparticles. The zero pressure (P_0) was set according to the point where fluorescent nanoparticles underwent Brownian motion inside the micropipette. The error in aspiration pressure (<2 Pa) was defined as the minimal pressure change near P_0 that resulted in an observable directed flow of fluorescent particles in the micropipette.

MPA experiments were carried out in glass-bottom dishes (ES56291, Azer Scientific, US) that were pre-treated with 5% Pluronic F-127 (P2443-250G, Sigma) for > 1 hour to prevent adhesion of RGG condensates to the glass*(1)*. Milli-Q water was added to the edge of the dish to minimize evaporation from the sample (Fig. 2a). We further quantified water evaporation rates under our experimental conditions using a 20 µL sample of Rhodamine-B solution (Fig. S2). Volume of the sample was assumed to be inversely proportional to its mean fluorescence intensity. No measurable volume change was observed when the dish-cap was on, providing a stable environment for necessary incubation periods for the sample. When the dish-cap was removed for micropipette aspiration, evaporation led to a slow constant decrease in the sample volume (~0.04 µL/min). We found that the evaporation can be compensated to be less than 5% in our MPA experiments (Fig. S2).

After calibration of the aspiration pressure, a 20~30 μL sample of phase separated protein solution was added to the center of the dish (Fig. 2a). Once micrometer-size protein condensates were observed at the bottom of the dish, a calibrated micropipette was moved to a condensate of interest to start the aspiration measurements. First, a positive (suction) pressure was applied to initiate the flow of the condensate into the micropipette. The condensate was typically allowed to flow into the micropipette until the aspiration length reached ~40 μm (the maximal aspiration length was limited by the field of view of the camera, initial condensate size, and the exact angle of the micropipette tip). Then, sequential stepwise ejection and suction pressures were applied to deform the condensate at different shear stresses while maintaining the aspiration length to be between 5 to 40 μm (Fig. 3b and S3a-b). The deformation of the condensate was recorded using a 60X objective, at 1 Hz (ORCA-Flash 4.0, Hamamatsu, Japan), either through transmitted light imaging (Fig. S1, S4, Movie S3) or through imaging the fluorescence of the EGFP tag (Fig. 3, S3, Movies S1, S2). The shape parameters of the aspirated condensates (L_p, R_p, R_c, H) were tracked using ImageJ. For data collected in the fluorescent channel, a MATLAB (R2019a) code was developed to automate the tracking of L_p. In the case of pipette-adhered condensates, we used the shape of the non-adherent part as an approximate for R_c.

To neglect potential nonlinear effect due to dissipation of the condensate flow in the pipette, the volume of condensate inside the micropipette is always around or below 5% of the volume of condensate outside the pipette. Larger condensates also lead to more accurate MPA measurements, because of the smaller perturbation of the changing aspiration length to R_c. For a condensate that is larger than 10 μm in radius, typical changes in aspiration length correspond to a < 3% change in R_c. For these reasons, in our experiments, small condensates were first manipulated into a large condensate through either a micropipette or an optical trap (see "**Optical trap mediated condensate fusion**" section) before MPA measurements.

When the RGG condensate first entered the micropipette, wetting between protein and glass led to dramatic changes in the interfacial curvature between the condensate and buffer inside the micropipette. The interfacial curvature stabilized in later steps (Fig. S3a, Movie S1). As a result, the P_{asp} vs. S relation during the initial-entry largely deviated from that of the remaining steps (Fig. S3b, S3c). We corrected for the change in H by subtracting a time-dependent P_γ from the aspiration pressure (Fig. S3d). However, the irreversible binding of a trace amount of protein to the inner wall of the aspiration pipette significantly accelerated the deformation of condensates during the initial-entry steps (Fig. S3e, S3f). To account for the lack of information about the kinetics of protein-glass binding, we disregarded the measurements from the initial-entry steps.

After the initial steps, the interfacial curvature between RGG condensates and buffer in the micropipette was set by the wetting of the protein to the inner pipette wall (Movie S1). Due to this wetting effect, RGG condensates flowed into the micropipette under both positive (suction) and small negative (ejection) pressures, whereas decreases in aspiration length only happened under large negative (ejection) pressures (Fig. 3, Movie S1, Fig. S4).

Viscosity of dextran-rich condensates

To calibrate the viscosity measurements, MPA should be applied to condensates with viscosity values that can be easily determined through other means. Dextran-rich condensates in a PEG-dextran aqueous two-phase system were chosen for this purpose (Fig. 2). After MPA, two independent methods were used to measure the viscosity of the dextran-rich phase.

1. Optical dragging

   An optical trap (Tweez305, Aresis, Slovenia) was applied to drag an r = 1.60 μm radius polystyrene bead (HUP-30-5, Spherotech, US) in a large dextran-rich condensate at 13 different velocities (Fig. 2e). The slope of the dragging force (f) vs. dragging speed (v) was used to calculate the viscosity (η) based on the Stokes equation (Equation S4):

$$\frac{df}{dv} = \eta \cdot 6\pi r \qquad \text{(S4)}$$

The measured viscosity was 74 ± 4 mPa·s. The stiffness of the optical trap (~ 0.02 pN/nm) was calibrated before each experiment by applying equipartition theorem to the thermal fluctuation of a trapped bead in the dextran-rich phase *(3)*.

2. Ubbelohde viscometer

After the bulk-phase separation of 40 ml PEG-dextran mixture, the bottom layer, corresponding to the dextran-rich phase, was applied through an Ubbelohde viscometer (13-614C, Cannon Instrument, US). The viscosity was measured to be 80 mPa·s.

Optical trap mediated condensate fusion

Two RGG condensates were individually controlled by two independent optical traps (Tweez305, Aresis, Slovenia) equipped on the Ti2-A inverted microscope (Nikon, Japan). As illustrated in Fig. 4a, the right condensate was moved towards the left one until they touched. Then, the right optical trap was turned off, and the condensates were allowed to fuse under the combined influence of their viscosity and surface tension. The fusion processes were acquired at a frame rate of 20 Hz using a 60x water objective. The acquired images were analyzed in MATLAB. The images were fitted into a Gaussian ellipse and the ratio of the major to minor axes of the ellipse (aspect ratio) was plotted as a function of time. The fusion time (τ) was extracted by fitting the change in the aspect ratio (*AR*) of fusing condensates to a single exponential decay (Fig. 4b, Equation S5).

$$AR = 1 + (AR_0 - 1)\mathrm{e}^{-t/\tau} \qquad \text{(S5)}$$

The length of condensates was defined as the geometric mean of the condensate diameters before fusion *(4)*. The ratio of viscosity to surface tension (inverse capillary velocity) was estimated from the slope of the fusion time vs. length relation (Fig. 4c).

Here, we chose the simple exponential fitting (eq. S5) to be consistent with the commonly-used routine in the literature *(4-9)*. We noticed that a stretched-exponential equation $AR = 1 + (AR_0 - 1)\mathrm{e}^{(-t/\tau)^{1.5}}$ can marginally improve the fitting quality to our fusion kinetics data (Fig. 4b), similar to the observation in a recent study *(10)*. The fitted fusion time τ, and therefore the inverse capillary velocity, were not significantly different from the values presented in Fig. 4c.

FRAP measurement of the condensate viscosity

FRAP experiments were performed on a total internal reflection fluorescence microscope (DMi8 TIRF, Leica, Germany) equipped with an Infinity Scanner system (Leica, Germany). All images were acquired using a 100X oil objective at 1 Hz. A 1.5 μm radius circular region was photobleached at the center of large RGG condensates (radius 9 ± 2 μm) using a short pulse (~1 s) of focused 488 nm laser, and the fluorescence recovery was analyzed using ImageJ. After background subtraction, fluorescence of the bleached region (I_{ROI}) was divided by the fluorescence of the entire condensate (I_{cond}) according to Equation S6, to minimize photobleaching and boundary effects *(11, 12)*.

$$I(t) = \frac{I_{ROI}(t) - I_{background}(t)}{I_{cond}(t) - I_{background}(t)} \qquad \text{(S6)}$$

The time point right after the bleaching step was defined as time zero. $I(t)$ was normalized so that the average of $I(t < 0)$ equals to 1.

To extract the half-recovery time, $I(t)$ was fitted to Equation S7a or Equation S7b, depending on whether an immobile fraction was included in the model.

$$I(t) = \frac{I_0 + I_\infty \frac{t}{\tau_{1/2}}}{1 + \frac{t}{\tau_{1/2}}} \qquad \text{(S7a)}$$

$$I(t) = \frac{I_0 + \frac{t}{\tau_{1/2}}}{1 + \frac{t}{\tau_{1/2}}} \qquad \text{(S7b)}$$

Here, $\tau_{1/2}$ is the half-recovery time and I_∞ is the mobile fraction (in Equation S7b, I_∞ is set to 1). For the FRAP measurements in this study (Fig. 4d), $\tau_{1/2}$ = 12.4 ± 0.5 s and I_∞ = 0.928 ± 0.003 when fitted to Equation S7a, while $\tau_{1/2}$ = 24 ± 1 s, when fitted to Equation S7b. Fittings were carried out in OriginPro 2020.

The diffusion coefficient (*D*) of the bleached molecule (RGG-EGFP-RGG) can be determined from a 2D or a 3D infinity model, according to Equation S8a or S8b, respectively *(11)*.

$$D = \frac{0.22 \cdot {r_{ROI}}^2}{\tau_{1/2}} \qquad \text{(S8a)}$$

$$D = \frac{0.1 \cdot {r_{ROI}}^2}{\tau_{1/2}} \qquad \text{(S8b)}$$

Where r_{ROI} = 1.5 μm is the radius of the bleached area, $\tau_{1/2}$ is the recovery time from Equation S7.

The viscosity of RGG condensates was then calculated using the Stokes-Einstein relation (Equation S9).

$$\eta = \frac{k_B T}{6\pi R_H D} \qquad \text{(S9)}$$

R_H is the hydrodynamic radius of RGG-EGFP-RGG. Using the online Hydrodynamic Radius Converter (https://www.fluidic.com/resources/Toolkit/hydrodynamic-radius-Converter/), R_H was estimated to be 6.54 nm, by taking into consideration the molecular mass and folding of RGG-GFP-RGG*(13)*.

Data availability

MATLAB codes used for quantitative data analysis in this study are available upon request.

Supplementary Figures

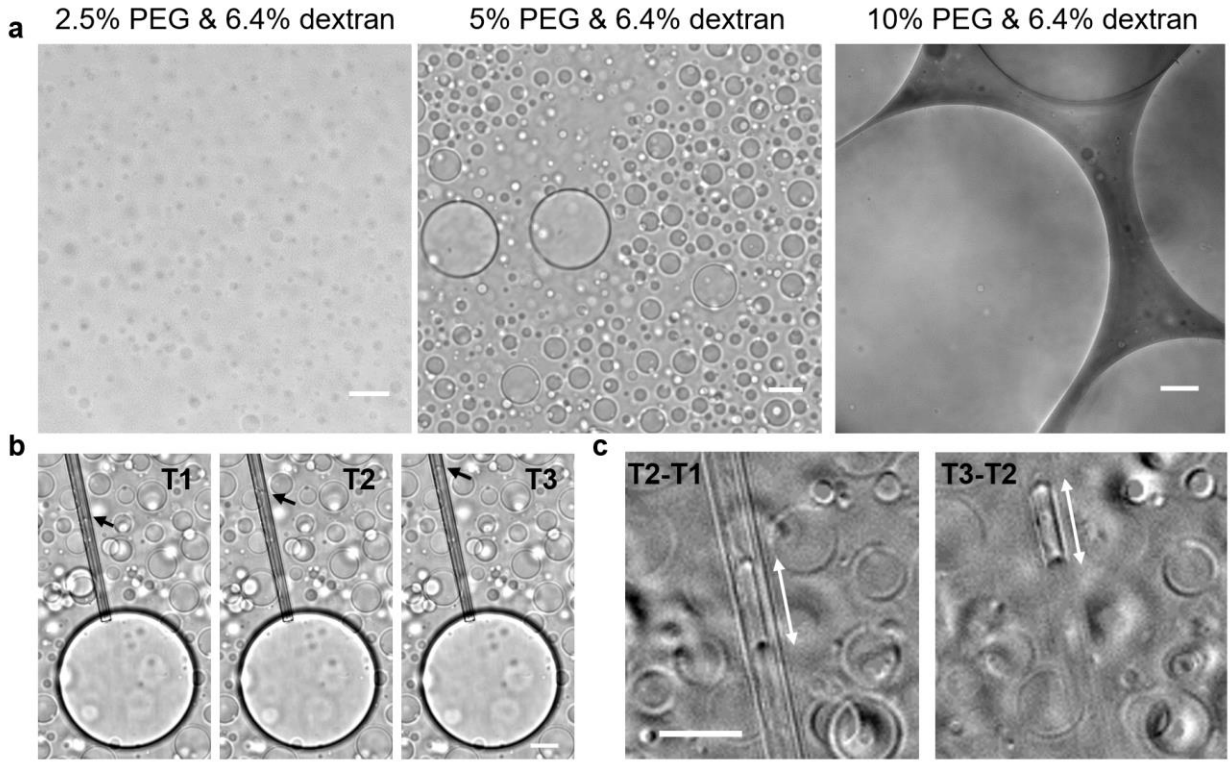

Figure S1: Phase separation and micropipette aspiration analysis of PEG and Dextran mixtures.
a, Micrometer-scale droplets were observed in emulsions of PEG-dextran. Left to right: mixtures of PEG (8,000 Da) and dextran (500,000 Da) at increasing ratios of PEG to dextran. The 5% PEG & 6.4% dextran condition was chosen to produce droplets with similar sizes to those of protein condensates. **b**, Flow of a dextran-rich condensate into a micropipette (pre-filled with PEG-rich solution) under constant suction pressure (60 Pa). The 3 images were taken at 3 seconds apart. Arrows point to the interfaces between the dextran-rich and PEG-rich phases which are zoomed-in in **c**. **c**, Intensity differences between images in **b**: T2-T1 (left) and T3-T2 (right). The double-arrows show the increase of aspiration length in 3 seconds. Analysis of the MPA experiment can be achieved as long as the condensate-buffer interface is resolvable. All scale bars, 20 µm.

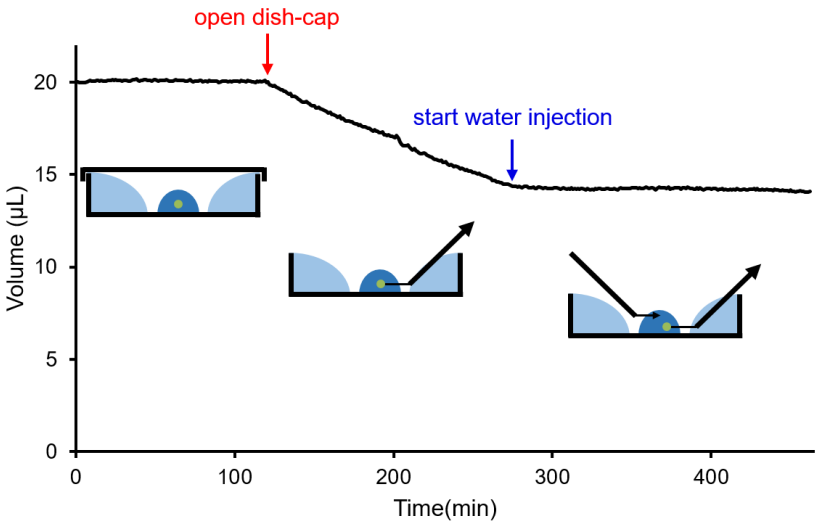

Figure S2: Quantification and correction of water evaporation during micropipette aspiration experiments.
Under our experimental conditions, the presence of peripheral water eliminated evaporation from the 20 µL sample as long as the cap of sample dish was on. Upon removing the cap (red arrow) for micropipette aspiration, water slowly evaporated at a rate of 0.04 µL/min. The evaporation during micropipette aspiration was compensated (blue arrow) through continuous injection of pure water using a second micropipette, or by adding 2 µL of pure water every 50 min. Sample volume was measured through fluorescence-based concentration measurement of Rhodamine-B at an imaging rate of 1 frame per minute and no measurable photobleaching was observed.

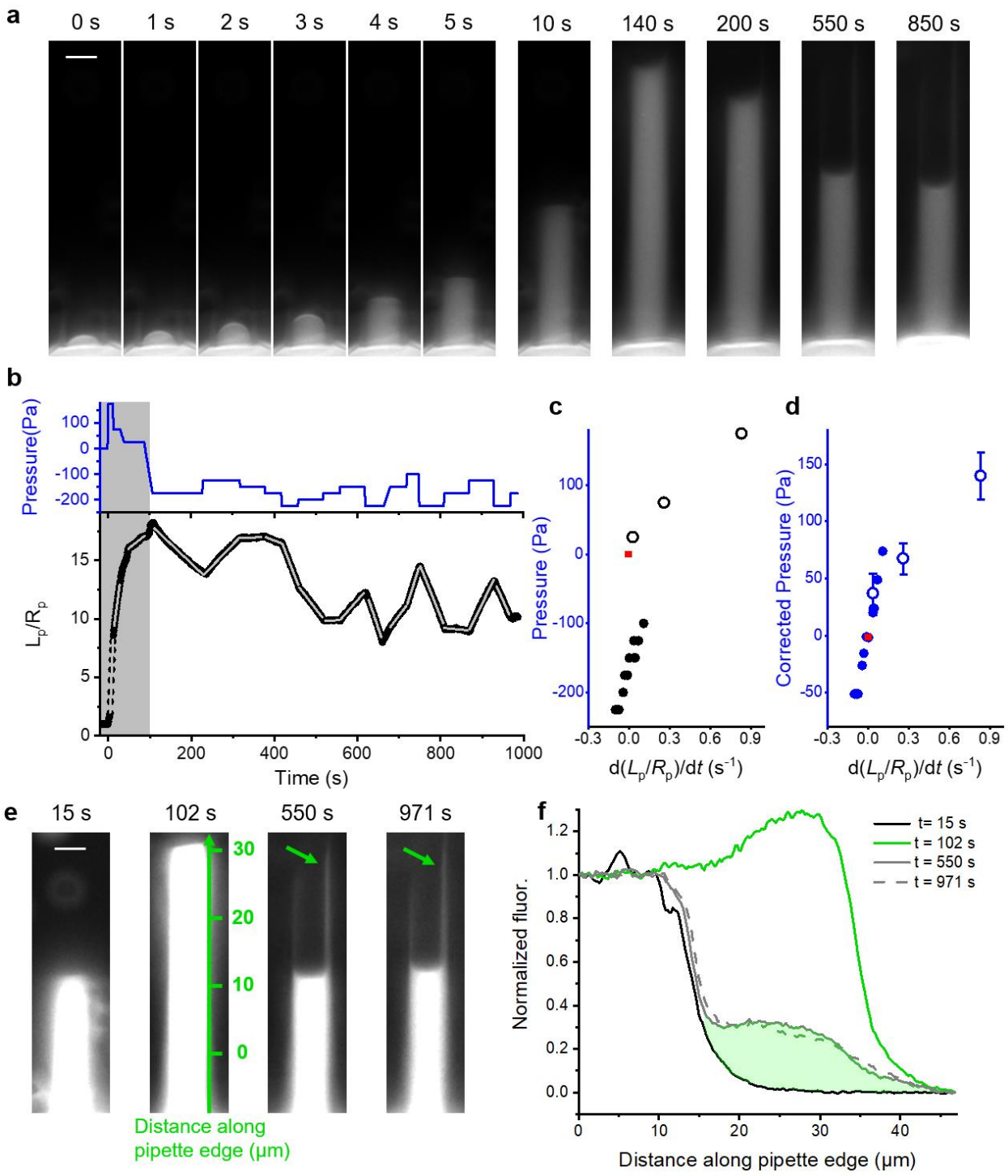

Figure S3: The interfacial curvature and the wetting of RGG condensate inside micropipette.

a, Time lapse fluorescence images showing the aspirated portion of the condensate. After proteins enter the micropipette (1- 4 s), the wetting of proteins to the inner pipette wall led to swift changes in the interfacial curvature of the protein condensate. In the case of RGG, this curvature stabilized within 2 min and remained near -1/R_p in the following aspiration steps. **b**, Aspiration

pressure (upper) and normalized aspiration length (lower) as a function of time. Shaded area represents the initial-entry steps (defined as when the protein condensate first encountered a bare glass micropipette), where irreversible binding of protein to pipette inner wall happens. Gray lines are linear fits to the normalized aspiration length under each pressure step. **c-d**, Raw aspiration pressure (**c**) and tension-corrected pressure (**d**) of each step plotted against the normalized deformation rate (slopes of the gray lines in **b**). The initial-entry steps are denoted by open circles and a red square is placed at (0,0). Error bars in **d** reflect the uncertainty in interfacial curvature during the initial-entry steps. **e**, Over-exposed images of the aspirated portion during (15 s, 102 s) and after (550 s, 971 s) the initial-entry steps. The axis (at 102 s) represents the edge of the micropipette, arrow (at 550 s) points to proteins that were stuck to the inner pipette wall, which persisted in further aspiration steps (arrow at 971 s). **f**, Line profile along the pipette edge at the four time points shown in **e**. Area of the shaded region shows the amount of protein that was stuck on the inner wall of the micropipette. All scale bars, 5 μm.

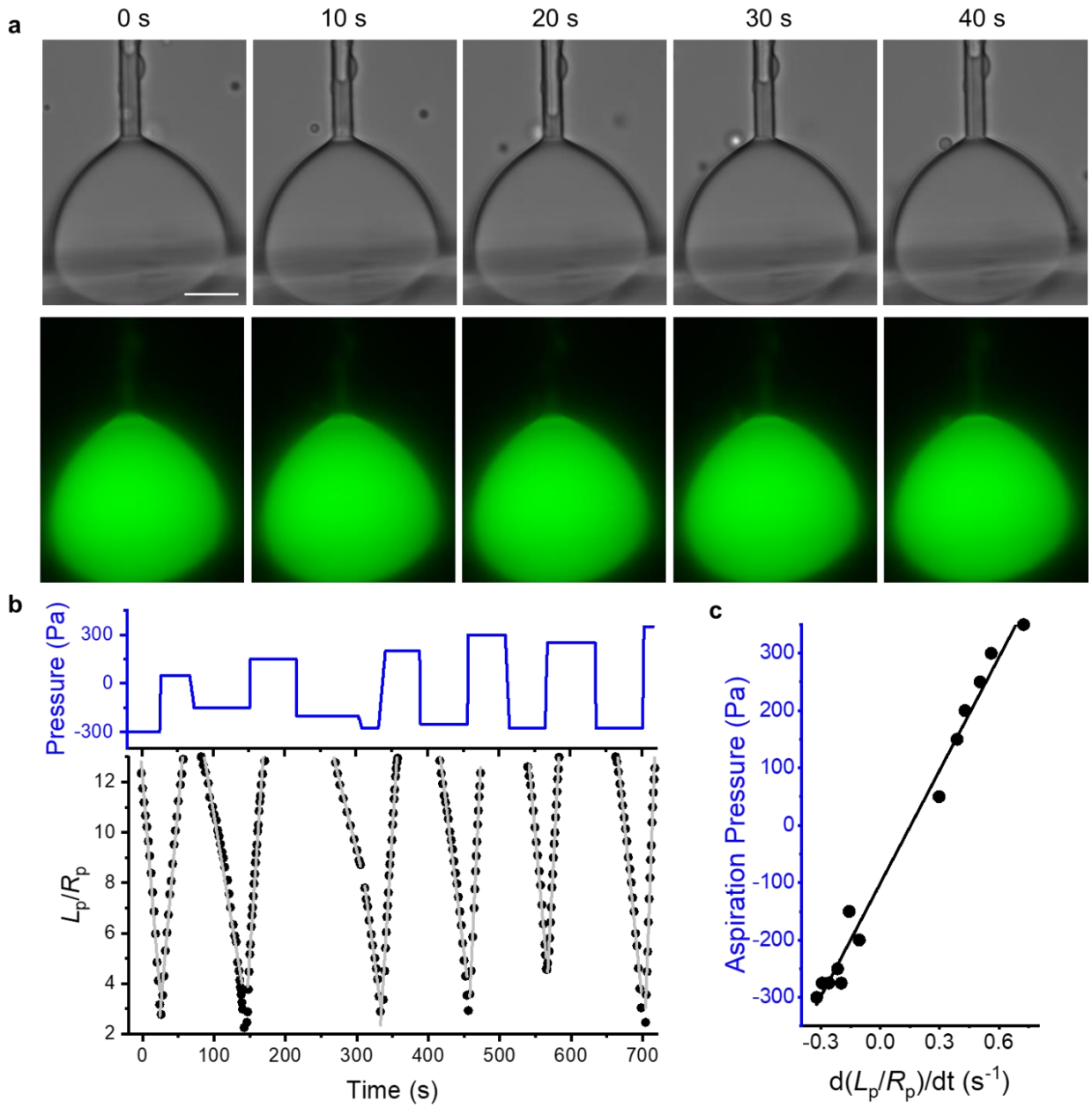

Figure S4: Micropipette aspiration analysis of RGG condensates under transmitted light. **a**, Time lapse transmitted (upper) and fluorescence (lower) images of an RGG condensate (adhered to a second pipette) under sequential ejection (-300 Pa, 0~20 s) and suction pressures (50 Pa, 20~40 s). **b**, Aspiration pressure (upper) and normalized aspiration length (lower) quantified from the transmitted light images. Gray lines: linear fits of the normalized aspiration length for each pressure step. **c**, P_{asp} of each step plotted against V (slopes of the gray lines in **b**). The black line represents a linear fit (slope: 660 ± 30 Pa·s, intercept: -100 ± 10 Pa, $R^2 = 0.985$). Scale bars, 10 µm.

Captions for Supplementary Movies

Movie S1: Micropipette aspiration of an RGG condensate free from adhesion to glass surfaces.

Movie S2: Micropipette aspiration of an RGG condensate strongly adhered to a glass pipette.

Movie S3: Micropipette aspiration of an RGG condensate imaged with transmitted light.

Supplementary Table

Liquid condensate	Viscosity (Pa·s) and method	Surface tension (mN/m) and method	Note
PGL-1*(4)*	~1 FRAP	~10^{-3} Fusion	Order of magnitude estimates
LAF-1*(14)*	23.4 SPT	0.19 Fusion	Average over RNA concentrations
Whil3*(15)*	15 FRAP and SPT	5 x 10^{-5} Fusion	Average over RNA concentrations
NPM1*(6)*	0.74 FRAP and SPT	8 x 10^{-4} Fusion and Sessile drop	
NPM1(*in vivo*) *(6)*	37 FRAP	4 x 10^{-4} Fusion and Sessile drop	
FIB1*(6)*	100 FRAP and SPT	1.23 x 10^{-3} Fusion and Sessile drop	
PGL-3*(16, 17)*	1 to 10^{4} Dual-OT	~4.5 x 10^{-3} Dual-OT	The viscosity increased significantly over time
FUS*(16)*	0.7 to 50 Dual-OT	~3.1 x 10^{-3}* Dual-OT	The viscosity increased significantly over time
Poly K*(18)*	0.204 FRAP and SPT	0.017 Fusion	
Poly R*(18)*	14.4 FRAP and SPT	0.1 Fusion	
[RGRGG]$_5$-dT40*(8)*	3 SPT and FCS	0.8 Fusion-OT	Average over salt concentrations
Glycinin*(19)*	~1600 Fusion	~0.16 Estimate	Surface tension $\gamma \sim k_B T/d^2$, where d is the size of glycinin
Cell Nucleus*(20)*	3000 Surface fluctuation	1.5 x 10^{-3} Fusion	
Double-Hydrophilic Block Copolymers*(21)*	*0.004* *FRAP*	*~5 x 10^{-5}* *Fusion*	*Not included in the plot of Figure 1*
Dextran-PEG*(22-24)*	0.023~0.17 Viscometer	0.01~0.1 Pendant drop Spinning drop tensiometer	At compositions similar to sample used in this study
Olive oil*(25, 26)*	0.0741 Viscometer	23.6 Pendent drop	All measured in water
Silicon oil*(27)*	0.02 Viscometer	36 Bubble contour	
Mineral oil*(28)*	7.75 x 10^{-3} Viscometer	49 Tensiometer	
$C_{16}H_{34}$ *(29)*	2.77 x 10^{-3} Viscometer	55.2 Tensiometer	
$C_{16}H_{34}$ with surfactants*(30)*	Assumed to be the same as above	Lowest to ~ 0.3 Tensiometer	
$C_{10}H_{22}$ *(29)*	9 x 10^{-4} Viscometer	53.2 Tensiometer	
C_6H_{14} *(29)*	3.13 x 10^{-4} Viscometer	51.4 Tensiometer	

Table S1: Literature values, methods, and references for data presented in Figure 1
FRAP: fluorescence recovery after photobleaching. **SPT**: single particle tracking. **Fusion**: first, a ratio of surface tension to viscosity was estimated from the fusion kinetics between two condensates. Then, a separate measure of viscosity was used to calculate surface tension values. Fusion experiments carried out using optical traps were noted as Fusion-OT. **Sessile drop**: a prism was used to image condensates

of various sizes from the side. The shape is determined by surface tension and gravity of the condensate. A separate measure of condensate density was used to extract surface tension. **Dual-OT**: Dual optical traps were used to periodically stretch a condensate via two bead-handles. Viscoelasticity of the condensate was measured via the phase delay of the strain relative to the stress. Surface tension was estimated from the elasticity of condensates.
** Surface tension value of FUS condensates was kindly provided by Dr. Frank Jülicher via email*

Supporting References

1. Schuster, B. S.; Reed, E. H.; Parthasarathy, R.; Jahnke, C. N.; Caldwell, R. M.; Bermudez, J. G.; Ramage, H.; Good, M. C.; Hammer, D. A. Controllable protein phase separation and modular recruitment to form responsive membraneless organelles. *Nature communications* **2018***, 9*, 1-12.

2. Riedstra, C. P.; McGorty, R. Liquid–Liquid Phase Separation: Undergraduate Labs on a New Paradigm for Intracellular Organization. *The Biophysicist* **2020***, 1*.

3. Osterman, N. TweezPal–optical tweezers analysis and calibration software. *Comput. Phys. Commun.* **2010***, 181*, 1911-1916.

4. Brangwynne, C. P.; Eckmann, C. R.; Courson, D. S.; Rybarska, A.; Hoege, C.; Gharakhani, J.; Jülicher, F.; Hyman, A. A. Germline P granules are liquid droplets that localize by controlled dissolution/condensation. *Science* **2009***, 324*, 1729-1732.

5. Brangwynne, C. P.; Mitchison, T. J.; Hyman, A. A. Active liquid-like behavior of nucleoli determines their size and shape in Xenopus laevis oocytes. *Proceedings of the National Academy of Sciences* **2011***, 108*, 4334-4339.

6. Feric, M.; Vaidya, N.; Harmon, T. S.; Mitrea, D. M.; Zhu, L.; Richardson, T. M.; Kriwacki, R. W.; Pappu, R. V.; Brangwynne, C. P. Coexisting liquid phases underlie nucleolar subcompartments. *Cell* **2016***, 165*, 1686-1697.

7. Agudo-Canalejo, J.; Schultz, S. W.; Chino, H.; Migliano, S. M.; Saito, C.; Koyama-Honda, I.; Stenmark, H.; Brech, A.; May, A. I.; Mizushima, N.; Knorr, R. L. Wetting regulates autophagy of phase-separated compartments and the cytosol. *Nature* **2021***, 591*, 142-146.

8. Alshareedah, I.; Thurston, G. M.; Banerjee, P. R. Quantifying viscosity and surface tension of multicomponent protein-nucleic acid condensates. *Biophys. J.* **2021**.

9. Schuster, B. S.; Dignon, G. L.; Tang, W. S.; Kelley, F. M.; Ranganath, A. K.; Jahnke, C. N.; Simpkins, A. G.; Regy, R. M.; Hammer, D. A.; Good, M. C. Identifying sequence perturbations to an intrinsically disordered protein that determine its phase-separation behavior. *Proceedings of the National Academy of Sciences* **2020***, 117*, 11421-11431.

10. Ghosh, A.; Zhou, H. Determinants for Fusion Speed of Biomolecular Droplets. *Angewandte Chemie International Edition* **2020***, 59*, 20837-20840.

11. Taylor, N. O.; Wei, M.; Stone, H. A.; Brangwynne, C. P. Quantifying dynamics in phase-separated condensates using fluorescence recovery after photobleaching. *Biophys. J.* **2019***, 117*, 1285-1300.

12. Shi, Z.; Graber, Z. T.; Baumgart, T.; Stone, H. A.; Cohen, A. E. Cell membranes resist flow. *Cell* **2018***, 175*, 1769-1779. e13.

13. Armstrong, J. K.; Wenby, R. B.; Meiselman, H. J.; Fisher, T. C. The hydrodynamic radii of macromolecules and their effect on red blood cell aggregation. *Biophys. J.* **2004***, 87*, 4259-4270.

14. Elbaum-Garfinkle, S.; Kim, Y.; Szczepaniak, K.; Chen, C. C.; Eckmann, C. R.; Myong, S.; Brangwynne, C. P. The disordered P granule protein LAF-1 drives phase separation into droplets with tunable viscosity and dynamics. *Proceedings of the National Academy of Sciences* **2015***, 112*, 7189-7194.

15. Zhang, H.; Elbaum-Garfinkle, S.; Langdon, E. M.; Taylor, N.; Occhipinti, P.; Bridges, A. A.; Brangwynne, C. P.; Gladfelter, A. S. RNA controls PolyQ protein phase transitions. *Mol. Cell* **2015***, 60*, 220-230.

16. Jawerth, L.; Fischer-Friedrich, E.; Saha, S.; Wang, J.; Franzmann, T.; Zhang, X.; Sachweh, J.; Ruer, M.; Ijavi, M.; Saha, S.; Mahamid, J.; Hyman, A. A.; Jülicher, F. Protein condensates as aging Maxwell fluids. *Science* **2020***, 370*, 1317-1323.

17. Jawerth, L. M.; Ijavi, M.; Ruer, M.; Saha, S.; Jahnel, M.; Hyman, A. A.; Jülicher, F.; Fischer-Friedrich, E. Salt-dependent rheology and surface tension of protein condensates using optical traps. *Phys. Rev. Lett.* **2018***, 121*, 258101.

18. Fisher, R. S.; Elbaum-Garfinkle, S. Tunable multiphase dynamics of arginine and lysine liquid condensates. *Nature Communications* **2020***, 11*, 1-10.

19. Chen, N.; Zhao, Z.; Wang, Y.; Dimova, R. Resolving the Mechanisms of Soy Glycinin Self-Coacervation and Hollow-Condensate Formation. *ACS Macro Letters* **2020***, 9*, 1844-1852.

20. Caragine, C. M.; Haley, S. C.; Zidovska, A. Surface fluctuations and coalescence of nucleolar droplets in the human cell nucleus. *Phys. Rev. Lett.* **2018***, 121*, 148101.

21. Lira, R. B.; Willersinn, J.; Schmidt, B. V.; Dimova, R. Selective Partitioning of (Biomacro) molecules in the Crowded Environment of Double-Hydrophilic Block Copolymers. *Macromolecules* **2020***, 53*, 10179-10188.

22. Atefi, E.; Mann Jr, J. A.; Tavana, H. Ultralow interfacial tensions of aqueous two-phase systems measured using drop shape. *Langmuir* **2014***, 30*, 9691-9699.

23. Carrasco, F.; Chornet, E.; Overend, R. P.; Costa, J. A generalized correlation for the viscosity of dextrans in aqueous solutions as a function of temperature, concentration, and molecular weight at low shear rates. *J Appl Polym Sci* **1989***, 37*, 2087-2098.

24. Liu, Y.; Lipowsky, R.; Dimova, R. Concentration dependence of the interfacial tension for aqueous two-phase polymer solutions of dextran and polyethylene glycol. *Langmuir* **2012***, 28*, 3831-3839.

25. Fisher, L. R.; Mitchell, E. E.; Parker, N. S. Interfacial tensions of commercial vegetable oils with water. *J. Food Sci.* **1985***, 50*, 1201-1202.

26. Sahasrabudhe, S. N.; Rodriguez-Martinez, V.; O'Meara, M.; Farkas, B. E. Density, viscosity, and surface tension of five vegetable oils at elevated temperatures: Measurement and modeling. *Int. J. Food Prop.* **2017***, 20*, 1965-1981.

27. Peters, F.; Arabali, D. Interfacial tension between oil and water measured with a modified contour method. *Colloids Surf. Physicochem. Eng. Aspects* **2013***, 426*, 1-5.

28. Kim, H.; Burgess, D. J. Prediction of interfacial tension between oil mixtures and water. *J. Colloid Interface Sci.* **2001***, 241*, 509-513.

29. Goebel, A.; Lunkenheimer, K. Interfacial tension of the water/n-alkane interface. *Langmuir* **1997***, 13*, 369-372.

30. Chen, H.; Han, L.; Luo, P.; Ye, Z. The interfacial tension between oil and gemini surfactant solution. *Surf. Sci.* **2004***, 552*, L53-L57.